https://doi.org/10.5194/egusphere-2026-3301
Preprint. Discussion started: 26 June 2026

Contrasting impacts of Asian sulfate aerosols on regional summer extreme precipitation under different climate backgrounds

Feifei Luo[1], Manoj Joshi[2], Bjørn H. Samset[3], Laura J. Wilcox[4], Camilla W. Stjern[3], Robert J. Allen[5], Yan-Ning Kuo[6], Wei Hua[1], and Shuanglin Li[7,8]

1. School of Atmospheric Sciences, Chengdu University of Information Technology, Chengdu, China
2. Climatic Research Unit, School of Environmental Sciences, University of East Anglia, Norwich, United Kingdom
3. CICERO Center for International Climate Research, Oslo, Norway
4. National Centre for Atmospheric Science, University of Reading, Reading, United Kingdom
5. Department of Earth and Planetary Sciences, University of California Riverside, Riverside, CA, United States of America
6. Department of Earth and Atmospheric Sciences, Cornell University, Ithaca, NY, United States of America
7. Climate Change Research Center, Institute of Atmospheric Physics, Chinese Academy of Sciences, Beijing, China
8. Department of Atmospheric Science, China University of Geoscience, Wuhan, China

Corresponding author: Feifei Luo (lff@cuit.edu.cn)

https://doi.org/10.5194/egusphere-2026-3301
Preprint. Discussion started: 26 June 2026

Abstract

This study investigates the impact of Asian sulfate aerosols on regional summer extreme precipitation under both pre-industrial and pre-industrial +1K climate states, using the reduced-complexity climate model Fast Ocean Rapid Troposphere Experiment version 2 (FORTE2) with Systematic Regional Aerosol Perturbations simulations. Results show that increased Asian sulfate aerosols reduce extreme precipitation, characterized by lower frequency and weaker intensity over East and South Asia in both climates, but the suppression is more pronounced over northern India in the +1K climate. Atmospheric energy budget analysis reveals this is primarily due to enhanced dynamic effects in the warmer climate. When aerosols are added to the pre-industrial climate state, an increased horizontal dry static energy (DSE) gradient partially offsets the aerosol-induced dynamic suppression over northern India. Under the +1K climate, higher atmospheric static stability weakens the local meridional circulation induced by aerosol forcing, reducing the meridional temperature gradient and thus diminishing the offsetting effect, making the dynamic suppression more dominant. Further analysis indicates that this difference in precipitation responses between the two climates results from the nonlinear effect between the aerosol-radiation and aerosol-cloud interactions under the +1K climate, whereas the two effects combine approximately linearly under the pre-industrial climate. This study suggests that continued global warming alone will exacerbate Asian sulfate aerosols' weakening of precipitation, including extremes, over northern India. This implies that future reductions in aerosol emissions may unmask or amplify extreme precipitation increases in this region.

https://doi.org/10.5194/egusphere-2026-3301
Preprint. Discussion started: 26 June 2026

1. Introduction

Extreme precipitation and its associated hydrometeorological and geological disasters, such as flooding, landslides, and debris flows, pose a serious threat to natural ecosystems and the safety of people's lives and property. This threat is exacerbated by global warming, which has increased the intensity and frequency of extreme precipitation on the global scale (IPCC, 2021). Anthropogenic aerosols, as a key driver of climate change, significantly influence extreme precipitation events, with effects comparable to, or even stronger than, those of greenhouse gases and internal variability in certain regions, including Asia (Lin et al., 2016; Samset et al., 2018; Guo et al., 2023; Iles et al., 2024).

Since the 1970s, anthropogenic aerosol emissions have increased substantially over East and South Asia due to rapid economic development. These emissions have significantly impacted the spatiotemporal changes in Asian summer monsoon rainfall through aerosol-radiation interactions (ARI) and aerosol-cloud interactions (ACI), as well as through associated large-scale circulation changes (e.g., Bollasina et al., 2011; Li et al., 2016; Tian et al., 2018; Luo et al., 2018; Dong et al., 2019; Wilcox et al., 2020; Monerie et al., 2022; Lang et al., 2025; Yang et al., 2026). During the rapid industrialization period, the aerosol emissions contributed to a reduction in heavy precipitation over China, partially offsetting the greenhouse gas-induced increase (Ma et al., 2017; Bai et al., 2024). However, the impacts of aerosols exhibit marked regional differences and uncertainties. For instance, Lin et al. (2018) have found that anthropogenic aerosols are a primary cause of reduced extreme precipitation over North China and India, mainly through ACI, which decreases cloud droplet effective radius and increases cloud droplet number concentration, thereby enhancing cloud albedo and cloud lifetime. This subsequently reduces surface solar radiation and temperature, weakening the land-sea thermal contrast and moisture transport. Guo et al. (2023) have shown that anthropogenic aerosol forcing is the dominant driver of increased summer extreme precipitation intensity and frequency in Northwest China, primarily through the dynamic enhancement of moisture flux convergence.

https://doi.org/10.5194/egusphere-2026-3301
Preprint. Discussion started: 26 June 2026

In recent decades, the sharp reduction in aerosol emissions over China has markedly accelerated the increase in extreme precipitation, primarily by increasing cloud droplet size and promoting more efficient droplet coalescence and precipitation (Zou et al., 2025). Under future scenarios, further aerosol emission reductions are expected to increase the extreme precipitation over the Asian monsoon region (Zhao et al., 2019; Wang et al., 2023). Global warming alters atmospheric water vapour, static stability, and cloud properties, all of which may influence aerosol-climate interactions. However, whether and how the influence of anthropogenic aerosols on Asian extreme precipitation varies with different climate backgrounds remains unclear. Understanding this question is helpful for more accurately projecting the future impact of anthropogenic aerosols on climate. In this study, we address this question by comparing idealized simulations of the same Asian anthropogenic sulfate aerosol perturbations under two distinct climate states using the coupled climate model FORTE2 (Fast Ocean Rapid Troposphere Experiment version 2). This model is of reduced complexity and well-suited for aerosol-climate studies, as it incorporates all the key mechanisms of aerosol-climate interactions and can efficiently run long simulations at low computational cost (Herbert et al., 2022; Stjern et al., 2024; Luo et al., 2025).

The rest of the paper is organized as follows. Section 2 describes the models and simulations, datasets, extreme precipitation indices, and methods. Section 3 first evaluates the model skill in simulating extreme precipitation, then examines the responses to Asian sulfate aerosol perturbations and the underlying mechanisms, and finally compares the differences between the two climate states and investigates the potential reasons. Section 4 provides a summary and discussion.

2. Models, Simulations and methods

2.1 The FORTE2 model and simulations

FORTE2 was developed as an intermediate-complexity coupled atmosphere-ocean general circulation model (Blaker et al., 2021). Its atmospheric module, the Intermediate General Circulation Model 4, operates at a T42 spectral resolution

https://doi.org/10.5194/egusphere-2026-3301
Preprint. Discussion started: 26 June 2026

corresponding to roughly 2.8° horizontally, with 35 sigma vertical levels extending up to 0.1 hPa (Joshi et al., 2015). This atmospheric component integrates full physical parameterizations for radiation, land-surface properties, convection, precipitation, and clouds schemes (Zhong and Haigh, 1995; Betts and Miller, 1993). For the oceanic component, the Modular Ocean Model-Array is adopted, featuring a 2°×2° horizontal grid with 15 vertical z-levels whose thickness increases with depth, ranging from 30 m at the sea surface to 800 m at the model bottom (Webb, 1996). Within the model system, sea ice functions as a thermal barrier restricting heat exchange between the ocean and atmosphere, and the coupled system runs without any flux adjustments terms.

Building on the FORTE2 platform, Stjern et al. (2024) designed and implemented a suite of Systematic Regional Aerosol Perturbations experiments, hereafter referred to as SyRAP-FORTE2. This experimental framework supports systematic investigation of climate impacts driven by aerosols from distinct geographic regions and of different chemical compositions, across various background climate scenarios. It also enables quantitative comparison between ARI and ACI effects, facilitating assessment of their respective contributions and potential interactive mechanisms. Instead of using aerosol emission or concentration fields as forcing inputs, a standard practice in most CMIP6 models including those participating in the Precipitation Driver and Response Model Intercomparison Project (PDRMIP) (Myhre et al., 2017), the SyRAP-FORTE2 simulations are forced by global gridded monthly aerosol optical depth (AOD) products with explicit vertical profiles, derived from the Copernicus Atmosphere Monitoring Service Reanalysis (CAMSRA) dataset (Inness et al., 2019).

Within the CAMSRA dataset, anthropogenic emissions for BC, organic carbon, and sulfur dioxide are sourced from the MACCity emission inventory for the 2003-2010 period, and switch to the Representative Concentration Pathway 8.5 emission scenarios from 2010 onward (Granier et al., 2011; Riahi et al., 2011). In the model setup, aerosols are assigned a vertically uniform distribution spanning from the second-lowest model layer, where σ (the ratio of grid pressure to surface pressure) equals approximately 0.88, corresponding to an altitude of around 950 m above the surface,

https://doi.org/10.5194/egusphere-2026-3301
Preprint. Discussion started: 26 June 2026

upward to a defined upper pressure boundary referred to as p_{min}. For each individual grid cell, the value of p_{min} is calculated from CAMSRA data as the lower of two thresholds: 850 hPa, or the lowest pressure level at which the 2003–2021 average mixing ratio of the combined BC, OC, and SO_4 mixture drops below 5×10^{-9} kg kg^{-1}. In areas with complex terrain, additional constraints are enforced to ensure σ_{min} remains below 0.75 and p_{min} stays above 300 hPa. To generate the regional AOD perturbation fields, monthly speciated AOD and three-dimensional mass mixing ratio data from CAMSRA (2003–2021) are first interpolated to match the T42 model resolution. Monthly climatologies are then computed for three AOD categories at each grid point: total anthropogenic aerosols (BC, OC, and SO_4), absorbing aerosols (BC and OC), and scattering aerosols (SO_4). These constructed idealized aerosol vertical profiles are subsequently input into FORTE2's radiation calculation scheme. Notably, FORTE2 does not include aerosol transport processes in its simulation configuration. A more detailed description of the aerosol implementation methodology in SyRAP-FORTE2 is available in Stjern et al. (2024).

The SyRAP-FORTE2 experiments used in this study include (Table 1): (1) two baseline simulations without aerosol forcing with CO_2 concentrations at pre-industrial levels (piC, 280 ppmv), and at a level (p1K, 500 ppmv) that yields a global-mean warming of approximately 1K relative to pre-industrial conditions in this model; (2) six perturbation simulations with SO_4 AOD forcing added over Asia (Fig. 1a), encompassing combined (ARI + ACI), ARI-only and ACI-only effects, all conducted under both the piC and p1K background climate states. All simulations were carried out over a 200-year period, with model years 51 through 200 used for the analysis. Subtracting each baseline from its corresponding perturbation isolates the climate effects of sulfate aerosol relative to a no-aerosol state, including the total (ARI+ACI) effect as well as the separate contributions from ARI and ACI. The impact of the background climate is then estimated by comparing these effects between the p1K and piC backgrounds, i.e., (SO_4_p1K-p1K) -(SO_4_piC-piC), which reveals how a warmer, higher-CO_2 climate modulates the sulfate-aerosol-induced responses examined here.

https://doi.org/10.5194/egusphere-2026-3301
Preprint. Discussion started: 26 June 2026

The ACI parameterization for sulfate perturbations is applied exclusively within the Asian study domain, which spans 60°–140° E and 0°–53° N (marked by the white box in Fig. 1a). The ACI effect is triggered once the local AOD value surpasses a threshold of 0.07. This threshold was selected based on observed relationships between AOD variations and cloud top effective radius changes reported in Dong et al. (2019). To represent the magnitude of ACI effects, the effective radius of cloud droplets is reduced from 15 μm to 10 μm across low-level clouds, mid-level clouds, and shallow convective clouds. The 5 μm reduction in droplet radius falls within the range of values simulated by the majority of CMIP5 models for this cloud property (Wilcox et al., 2015).

In this experimental design, both the sulfate AOD magnitude and its vertical profile are prescribed as fixed monthly climatologies, meaning they do not evolve or adjust in response to simulated climate variations. This idealized approach means that no feedbacks exist between the climate response and aerosol distribution (e.g., enhanced precipitation does not lead to increased aerosol removal), and also excludes any interactive atmospheric chemistry changes. As a result, any observed differences in sulfate-induced climate response between the p1K and piC backgrounds can be attributed entirely to differences in the background climate state (such as warmer temperatures, higher atmospheric water vapor content, and altered large-scale circulation patterns), rather than to variations in the strength or distribution of the aerosol forcing itself.

2.2 PDRMIP simulations

We also qualitatively compare the FORTE2 results with simulations from the PDRMIP (Myhre et al., 2017). Specifically, we use 10× present-day Asian SO_4 emissions/concentrations experiments from five global climate models (CESM1-CAM5, GISS-E2-R, HadGEM3, MIROC-SPRINTARS, and NorESM1; Table 2), each compared against its own year-2000 baseline experiment with present-day aerosols and greenhouse gases. The PDRMIP models are fully coupled earth system models and are substantially more comprehensive than the FORTE2 framework. Two important caveats should be noted. First, the PDRMIP simulations prescribe a much stronger SO_4

https://doi.org/10.5194/egusphere-2026-3301
Preprint. Discussion started: 26 June 2026

perturbation, with a regional summer multi-model mean (MMM) AOD value of ~2.5 over East Asia and South Asia compared to ~0.23 in FORTE2 (Fig. 1). Therefore, only the sign and spatial pattern, not the magnitude, of the responses should be compared, which would support the robustness of the FORTE2 results. Second, the PDRMIP experiments are conducted under a single background climate state and therefore cannot assess the influence of a warmer background climate, which is the central focus of the present study.

2.3 Reanalysis data and extreme precipitation index

To support observational comparison, daily precipitation records, monthly sea level pressure (SLP) fields, as well as monthly horizontal and vertical wind components were obtained from the fifth-generation ECMWF atmospheric reanalysis (ERA5). The dataset has a uniform horizontal grid spacing of 0.25° × 0.25° and covers the period from 1981 through 2010 (Hersbach et al., 2023a, b).

Following the standardized indicator framework put forward by the Expert Team on Climate Change Detection and Indices (ETCCDI), we derived four precipitation metrics for subsequent analysis. PRCPTOT (unit: mm) represents the cumulative precipitation sum across all wet days within the target season. R95p (unit: mm) denotes the total precipitation amount recorded exclusively on extremely wet days. R95d (unit: days) counts the total number of extremely wet days, and R95int (unit: mm/day) characterizes the average precipitation intensity of extreme events, calculated as the quotient of R95p divided by R95d. A wet day was defined as its daily precipitation reaches or exceeds 1 mm. The 95th percentile of wet-day daily precipitation is adopted as the threshold for extremely wet days, with separate baseline references for different data sources: for FORTE2 and PDRMIP simulations, the percentile threshold is computed from their corresponding baseline simulations; for the ERA5 reanalysis, the 1981–2010 period is used as the reference baseline to derive the threshold. All analyses in this study focus on boreal summer (June-August, JJA).

2.4 Atmospheric energy budget

To uncover the physical mechanisms driving precipitation changes, we employ an

https://doi.org/10.5194/egusphere-2026-3301
Preprint. Discussion started: 26 June 2026

atmospheric column energy budget framework, which partitions precipitation-related energy variations into a thermodynamic component (denoted Q) and a dynamic component (denoted H) (Muller and O'Gorman, 2011; Richardson et al., 2016; Liu et al., 2018). In this framework, the latent heat release associated with precipitation changes (LcδP) is balanced by changes in net atmospheric diabatic cooling (δQ) and dry static energy (DSE) flux divergence (δH), as expressed in Eq. (1):

$$L_c\delta P = \delta Q + \delta H \quad (1)$$

where L_c is the latent heat of condensation, P stands for precipitation, and δ denotes the change relative to the reference baseline simulation. The term δQ is calculated by summing variations in three factors: atmospheric longwave cooling, atmospheric shortwave absorption, and surface sensible heat flux. Correspondingly, δH is derived as the residual value obtained by subtracting δQ from LcδP.

The total DSE flux divergence anomaly δH is further divided into a time-mean component (δH_m) and a transient eddy component (δH_{trans}), as shown in Eq. (2): $\delta H = \delta H_m + \delta H_{trans}$ (2)

δH_m can be broken down into four distinct terms, which correspond to the dynamic and thermodynamic effects on vertical and horizontal DSE advection respectively. The full decomposition is presented in Eq. (3):

$$\begin{aligned}\delta H_m &= \delta H_{Dy\_v} + \delta H_{Th\_v} + \delta H_{Dy\_h} + \delta H_{Th\_h} \\ &= \int \delta\overline{\omega}\frac{\partial\overline{s}}{\partial p}\frac{dp}{g} + \int \overline{\omega}\delta\left(\frac{\partial\overline{s}}{\partial p}\right)\frac{dp}{g} + \int \delta\overline{u} \bullet \nabla\overline{s}\frac{dp}{g} + \int \overline{u} \bullet \delta(\nabla\overline{s})\frac{dp}{g}\end{aligned} \quad (3)$$

where ω is vertical velocity, s is DSE, p is pressure, g is the gravitational acceleration, u is horizontal wind vector, ∇ is the horizontal gradient, and an overbar indicates climatological monthly means. Physically, δH_{Dy_v} reflects the dynamic effect arising from changes in vertical velocity; δH_{Th_v} corresponds to the thermodynamic effect induced by changes in vertical DSE gradients; δH_{Dy_h} represents the dynamic effect caused by changes in horizontal wind fields; δH_{Th_h} captures the thermodynamic effect related to changes in horizontal DSE gradients. Finally, δH_{trans} is calculated as a residual between δH and δH_m.

3. Results

https://doi.org/10.5194/egusphere-2026-3301
Preprint. Discussion started: 26 June 2026

3.1 Model evaluation

To understand the ability of the models to simulate precipitation patterns and large-scale circulation, we compare the FORTE2 p1K baseline and the PDRMIP year-2000 baseline simulations with ERA5 (1981–2010). In ERA5, R95p shows a spatial pattern similar to PRCPTOT, with maxima over northern India, Southeast Asia and South China (Fig. 2a and 2b). R95d is characterized by approximately five extremely wet days in tropical regions, and three in mid- to high-latitudes with maxima over Northwest China (Fig. 2c). The highest R95int values are concentrated over the Asian summer monsoon region (Fig. 2d). The PDRMIP MMM reasonably reproduces the observed spatial patterns of PRCPTOT and extreme precipitation, with pattern correlation coefficients exceeding 0.85 (Fig. 2e–h). The individual PDRMIP models show pattern correlations, with values ranging from 0.70 (GISS-E2-R) to 0.85 (HadGEM3) for PRCPTOT, 0.69 to 0.82 for R95p, 0.69 to 0.89 for R95d, and 0.64 to 0.80 for R95int, all of which are, as expected, lower than the MMM skill. FORTE2 exhibits relatively lower pattern correlation coefficients for PRCPTOT (0.56) and R95p (0.63), with notable dry biases over India (Fig. 2i and 2j). FORTE2 also shows a low pattern correlation coefficient of 0.39 for R95d, particularly in tropical regions (Fig. 2k). For R95int, FORTE2 achieves a pattern correlation coefficient of 0.68, indicating a reasonable representation of the spatial structure. These systematic discrepancies in FORTE2, particularly the dry biases and low spatial correlation for extreme wet days in the tropics, are likely due to the convective parameterization scheme employed in the model. However, it should be noted that some of the discrepancies may stem from the differing background climate states among the three datasets. The p1K simulation in FORTE2 has no aerosol and the CO_2 concentration slightly higher than present-day levels, whereas the aerosol and greenhouse gas forcing in PDRMIP is close to observation.

Both the PDRMIP MMM and FORTE2 reasonably simulate the basic summer atmospheric circulation patterns compared to ERA5, capturing the land-sea pressure gradient and the distributions of horizontal and vertical wind fields (Fig. 3). However,

https://doi.org/10.5194/egusphere-2026-3301
Preprint. Discussion started: 26 June 2026

FORTE2 simulates a much stronger continental low and a weaker western North Pacific Subtropical High relative to both the PDRMIP MMM and ERA5 (Fig. 3a-c). This difference likely reflects the strength of the trade winds, Hadley and Walker circulations in the model, which are closely tied to the untuned convective parameterizations and their coupling with SST. The simulated horizontal winds in FORTE2 show an excessive eastward extension of the westerlies over the western tropical Pacific and weakened easterlies over the tropical Pacific. Compared to ERA5, both the PDRMIP MMM and FORTE2 underestimate upward motion over the western tropical Pacific. Unlike ERA5 and the PDRMIP MMM, FORTE2 overestimates upward motion over the eastern Tibetan Plateau, corresponding to its wet precipitation biases in the region (Fig. 3d-f). Additionally, FORTE2 fails to simulate the upward motion over the tropical Indian Ocean seen in ERA5 and the PDRMIP MMM. These biases in the FORTE2 p1K simulation mirror those found in its piC simulation (Luo et al., 2025).

3.2 Responses to Asian sulfate aerosols and associated physical processes

The spatial patterns of precipitation indices in response to increased Asian sulfate aerosols are illustrated in figure 4 for the PDRMIP MMM and the SO_4_p1K and SO_4_piC simulations in FORTE2. To intuitively reflect the magnitude of regional precipitation responses, relative changes in PRCPTOT, R95p and R95int with respect to the respective baseline simulations are shown here. It should be kept in mind that the sulfate perturbation in PDRMIP is roughly an order of magnitude stronger than the FORTE2 perturbation. Hence, the response magnitudes are expected to differ considerably between the two datasets. The PDRMIP MMM and the two FORTE2 simulations show significant reductions in PRCPTOT and R95p over East China and India, and enhancements over northwestern India (Fig. 4a-j), in response to increased sulphate, consistent with previous work (Liu et al., 2018). R95p exhibits a stronger response than PRCPTOT, suggesting that extreme precipitation is more sensitive to sulfate forcing than mean precipitation, consistent with Samset et al. (2018). The responses of R95d and R95int are similar to those of R95p, indicating that the reduction in R95p is characterized by a lower frequency and weaker intensity (Fig. 4c-l). While

https://doi.org/10.5194/egusphere-2026-3301
Preprint. Discussion started: 26 June 2026

FORTE2 is a model of lower complexity, its results show high agreement with the five PDRMIP models.

In general, the changes in extreme precipitation are consistent with those in total precipitation, despite differences in magnitude, suggesting that the decreases in mean and extreme precipitation share some common drivers, such as large-scale circulation changes. To the extent that this holds, understanding the mechanisms behind mean precipitation changes can shed light on those driving extreme precipitation changes. Figure 5 shows the area-averaged atmospheric column energy budget terms (see Eq. 1 -3) for East Asia and South Asia. In both regions, the responses of $L_c\delta P$ are nearly equal to the responses of δH in the PDRMIP MMM and FORTE2 simulations, a result that is consistent across the five PDRMIP models. δQ is relatively small compared to δH and remains close to zero in the MMM. Hence, the dynamic effects induced by Asian sulfate forcing play a dominant role in decreasing summer precipitation over East Asia and South Asia.

Further, δH can be decomposed into δH_m and δH_{trans}. δH_m comprises four terms: δH_{Dy_v}, δH_{Dy_h}, δH_{Th_v}, and δH_{Th_h}, which represent dynamic and thermodynamic contributions to vertical and horizontal DSE advection, respectively. For the PDRMIP MMM (gray bars in Fig. 5), δH_{Dy_v} shows relatively larger negative changes than the other terms over both regions, and thus serves as the primary contributor to δH. Over East Asia, δH_{Th_h} and δH_{trans} exhibit negative changes and contribute to δH, whereas δH_{Dy_h} provides a partial offset (Fig. 5a). Over South Asia, δH_{Th_v} and δH_{Dy_h} act as negative contributors to δH, while δH_{trans} partially counteracts this reduction (Fig. 4b). However, some differences exist among the PDRMIP models. For instance, the contribution of δH_{trans} in NorESM1 (green asterisk) exceeds that of δH_m over East China, which is opposite to the results in the other two models (purple triangle and blue cross) (Fig. 5a).

3D atmospheric outputs from FORTE2 were archived at three pressure levels (250 hPa, 500 hPa, and 850 hPa), allowing identification of the leading term within δH_m. In

https://doi.org/10.5194/egusphere-2026-3301
Preprint. Discussion started: 26 June 2026

the FORTE2 simulations (blue and green bars in Fig. 5), the remaining three terms are consistently smaller in magnitude than δH_{Dy_v} in both simulations, a finding that aligns with the PDRMIP MMM results. Hence, the dynamic effect of vertical circulation (δH_{Dy_v}) is the dominant driver of the precipitation reduction over both East China and India.

Figure 6 shows the spatial patterns of summer responses for the relevant variables in the PDRMIP MMM and in the SO_4_p1K and SO_4_piC simulations of FORTE2. The decrease in δH_{Dy_v} is associated with anomalous descent (Fig. 6a-c), accompanied by high-pressure SLP anomalies (Fig. 6d-f). These SLP anomalies result from surface cooling induced by enhanced AOD forcing (Fig. 6g-i), which reduces incoming shortwave radiation (SW) (Fig. 6j-l). The reduced SW partly results from direct scattering of SW through ARI, and partly from low cloud changes through ACI (Fig. 6m-n). The above analysis indicates that the responses to Asian sulfate forcing, along with the related physical processes simulated by FORTE2, agree with those of the PDRMIP models. The robustness of these responses confirms that FORTE2 provides a suitable tool for investigating precipitation responses under contrasting climate backgrounds.

3.3 Differences between the p1K and piC climate conditions and their potential causes

The precipitation responses to Asian sulfate forcing, in terms of both their spatial patterns and associated physical mechanisms, are consistent between the SO_4_p1K and SO_4_piC simulations (Fig. 4-6). Nevertheless, some differences in the magnitude of the response can be found between the two climate states. Specifically, no significant difference in PRCPTOT is seen between the response to sulfate in p1K and piC climate conditions over East Asia, whereas a significantly stronger suppression of precipitation is evident over northern India and northwestern China under the p1K conditions (Fig. 7a). The differences in R95p and R95int closely resemble those in PRCPTOT, but R95d exhibits no statistically significant change (Fig. 7b-d). Quantitatively, the response over

https://doi.org/10.5194/egusphere-2026-3301
Preprint. Discussion started: 26 June 2026

East Asia is slightly weaker under the p1K climate than under the piC climate, though these differences do not attain 90% statistical significance (Fig. 8a). Over South Asia, the increased Asian sulfate AOD forcing under the p1K conditions induces a substantially stronger fractional reduction than the equivalent forcing under the pre-industrial conditions, with differences of 14.5% for PRCPTOT, 20% for R95p, 12.1% for R95int (Fig. 8b). The differences in PRCPTOT, R95p, and R95int are statistically significant at the 95% confidence level. For R95d, the reduction is 0.1 day greater under p1K than under piC, though this difference is not statistically significant. This suggests that the differences in total precipitation result primarily from changes in extreme precipitation over northern India, manifesting as a pronounced reduction in intensity and a negligible reduction in frequency.

The atmospheric energy budget is used to investigate the potential mechanisms underlying the differing precipitation responses over northern India (65°-95°E, 20°-30°N; black box in Fig. 9b). As shown in figure 9a, differences in the dynamic effect (δH) are the primary cause of the corresponding precipitation differences. Furthermore, the greater reduction of δH in SO_4_p1K relative to SO_4_piC is largely attributable to an enhanced the horizontal DSE gradient (δH_{Th_h}) in SO_4_piC, which partially offsets the decreases in the other three terms. In contrast, SO_4_p1K exhibits a slight decrease in δH_{Th_h}, thereby contributing, albeit weakly, to the overall precipitation reduction. The other three terms show no significant differences between the two climate states. This contrast is further illustrated by the spatial distribution. In SO_4_piC, an amplified increase in δH_{Th_h} over northern India and a marked decrease over northwestern India are observed (Fig. 9c), whereas these features are considerably weaker in SO_4_p1K (Fig. 9b), consistent with the significant precipitation differences over northern India between the two experiments (Fig. 7a).

In SO_4_piC, the enhanced δH_{Th_h} over northern India is associated with the north – south surface temperature gradient (Fig. 10a). The warm anomalies over southern India are induced by decreased precipitation and subsidence (Fig. 10b), while the cold anomalies over northern India result from reduced surface SW caused by the

https://doi.org/10.5194/egusphere-2026-3301
Preprint. Discussion started: 26 June 2026

increased sulfate AOD forcing and enhanced convective cloud cover over northwestern India (Fig. 10c-d). The increased convection is linked to ascent triggered by the subsidence over southern India (Fig. 10c-d). Relative to SO_4_piC, SO_4_p1K exhibits weaker cold anomalies over northern India, corresponding to the weaker north–south surface temperature gradient (Fig. 10e) and δH_{Th_h} in SO_4_p1K. These weaker cold anomalies are consistent with reduced SW dimming, weaker ascent, and diminished convective cloud cover over northwestern India (Fig. 10f-h), indicating a dampened local meridional circulation in SO_4_p1K. This attenuation results from the increased lower troposphere stability in p1K compared to that in piC (Fig. 10i).

3.4 The role of ARI and ACI effects

Figure 11 shows the spatial patterns of precipitation response to Asian sulfate AOD forcing in the ARI-only and ACI-only simulations under the two climate states, as well as their differences between these states. In the ARI-only simulations, no significant precipitation responses are evident over India for PRCPTOT and R95p, except for a localized enhancement over northwestern India (Fig. 11a-b and 11d-e). Although the ARI effect exerts a negligible influence on the Indian summer precipitation, it nonetheless induces a discernible difference in the response between the two climate states, marked by a reduction, especially in R95p over northern India in p1K relative to piC (Fig. 11c and 11f).

In both climate states, the ACI effect suppresses total and extreme precipitation over most of India by increasing cloud albedo and lifetime (Fig. 11g-h and 11j-k), which is consistent with a previous study (Guo et al., 2015). This suppression is significantly weaker over northern India in p1K compared to piC (Fig. 11i). This weakened suppression is also evident in extreme precipitation, where it exhibits an even stronger response (Fig. 11l). Hence, the precipitation response to ACI is significantly weakened over northern India under a warmer and wetter background climate in FORTE2. This may be because abundant moisture or deep convection (Fig. 12a-b) enhances collision-coalescence efficiency or convective invigoration, promoting precipitation and offsetting the suppression (Rosenfeld et al., 2008; Chavez and Barros, 2023; Zhao et

https://doi.org/10.5194/egusphere-2026-3301
Preprint. Discussion started: 26 June 2026

al., 2025). Besides, the surface SW response to Asian sulfate AOD does not differ significantly between the two climate states (Fig. 12c), indicating that the weakened precipitation suppression in p1K is not due to a weaker radiative forcing, but rather to the modulating effect of the warmer and wetter background climate.

To explore whether the ARI and ACI effects combine linearly, we compare their sum with the combined simulation under the two background states (Fig. 13). Under the piC state, this sum exhibits a decrease in precipitation over India and an increase over northwestern India (Fig. 13a). This spatial pattern resembles that of the combined simulation (Fig. 13b), and the differences between the sum and the combined simulation are insignificant (Fig. 13c), suggesting that the ARI and ACI effects combine approximately linearly in this case. In contrast, under the p1K state, the sum shows an increase over northern India and a decrease over central India (Fig. 13d). Here, the differences relative to the combined simulation reveal a significant decrease over northeastern India (Fig. 13e), indicating a notable nonlinear interaction between ARI and ACI under this background state (Fig. 13f). The nonlinearity may arise because the ARI effect induces surface cooling, which reduces moisture through weakened evaporation, and reduces the Indian summer monsoon due to the weakened land–sea thermal contrast. These drier conditions may, in turn, favor the precipitation suppression by ACI. The mechanism remains hypotheses that warrant further exploration.

Consequently, the precipitation difference between the two climate states derived from the sum of the individual effects (Fig. 13a and 13b) is of opposite sign to the difference seen in the combined simulation (Fig. 7a). This disparity indicates the critical role of the nonlinear interaction between the ARI and ACI effects under the p1K state, in shaping the net precipitation differences between the two climate states.

4. Conclusion

In this study, we have examined the responses of Asian summer mean and extreme precipitation to adding Asian sulfate aerosols, and investigated the differences in responses between the pre-industrial +1K (p1K) and pre-industrial (piC) climate

https://doi.org/10.5194/egusphere-2026-3301
Preprint. Discussion started: 26 June 2026

conditions and the associated physical mechanisms, using both the SyRAP simulations based on the reduced-complexity climate model FORTE2 and PDRMIP multi-model simulations. Our main findings are summarized as follows.

A comparison with the PDRMIP multi-model simulations demonstrates that FORTE2 reasonably reproduces the response of summer mean and extreme precipitation over Asia to regional sulfate forcing and its underlying physical processes. Increased Asian sulfate forcing significantly reduces the frequency and intensity of summer extreme precipitation over East Asia and South Asia. While the spatial patterns of these changes are consistent with those of mean precipitation, the magnitude of the response in R95p is considerably larger, suggesting that extreme precipitation exhibits heightened sensitivity to sulfate forcing relative to mean precipitation. Energy budget analysis reveals that precipitation reductions over East Asia and South Asia are driven predominantly by changes in DSE flux divergence (δH), with the dynamic vertical advection term (δH_{Dy_v}) identified as the leading contributor in both the PDRMIP MMM and FORTE2 simulations. Physically, this reflects anomalous descent associated with surface high-pressure anomalies induced by surface cooling via ARI and ACI effects. Although there is high agreement across the models, some differences exist, especially for changes in horizontal winds (δH_{Dy_h}) and the transient term (δH_{trans}). These differences may be related to the horizontal and vertical resolutions in the PDRMIP models.

The precipitation responses to same Asian sulfate AOD forcing exhibit consistent spatial patterns but divergent magnitudes between p1K and piC climates, with significantly stronger suppression over India under p1K conditions (14.5% for PRCPTOT, 20% for R95p). The difference manifests as a pronounced reduction in intensity (12.1% for R95int) but a negligible reduction in frequency. This enhanced response over northern India stems from differences in the dynamic response, specifically the horizontal DSE gradient term (δH_{Th_h}). In SO_4_piC, a stronger north–south temperature gradient amplifies δH_{Th_h} over northern India, thereby partially offsetting the precipitation reduction. However, under SO_4_p1K, increased lower-

https://doi.org/10.5194/egusphere-2026-3301
Preprint. Discussion started: 26 June 2026

tropospheric stability weakens the local meridional circulation and diminishes this offset, yielding a larger net reduction in precipitation.

The findings further reveal distinct roles of ARI and ACI under the two climate states. The ARI-only effect negligibly influences Indian summer precipitation, whereas the ACI-only effect consistently suppresses it. Notably, this ACI-induced suppression weakens significantly over northern India under the warmer, wetter p1K state relative to the cooler piC state, likely due to the more abundant moisture or stronger deep convection in the p1K state. Critically, these two effects combine linearly under piC but nonlinearly under p1K, suggesting a change in the ARI-ACI interaction under the background climate. Consequently, the precipitation difference between the two climate states derived from summing the individual ARI and ACI effects is of opposite sign to that obtained from the combined ARI and ACI simulation.

5. Discussion

These results indicate that under global warming, the background climate amplifies suppression of precipitation, including extreme events, by Asian sulfate aerosols over northern India through its influence on atmospheric stability and circulation strength. This amplification is independent of changes in the aerosol burden itself. If this modulating effect also holds for sulfate aerosol reductions and is approximately linear, northern India is likely to experience more severe extreme heavy precipitation events in the future. This is because ongoing reductions in sulfate aerosol emissions from air quality measures, particularly in East Asia, directly enhance precipitation, and continued global warming both intensifies precipitation directly and amplifies the precipitation increase driven by aerosol reductions.

This study underscores the strong dependence of aerosol–precipitation relationships on the background climate. However, FORTE2 is a simplified climate model, while it includes most of the key processes, certain limitations remain, such as the lack of wet deposition feedbacks, and biases in simulating the Indian summer precipitation. The findings reported here should therefore be tested with more comprehensive models to establish their robustness.

https://doi.org/10.5194/egusphere-2026-3301
Preprint. Discussion started: 26 June 2026

Acknowledgements. Some of the research presented in this paper was carried out on the High Performance Computing Cluster supported by the Research and Specialist Computing Support service at the University of East Anglia. We acknowledge the Center for Advanced Study in Oslo, Norway that funded and hosted our HETCLIF centre during the academic year of 2023/24. F. L. is supported by the National Natural Science Foundation of China (Grant 42305049). B. H. S., C. W. S., L. J. W., M. J. and R. J. A were supported by the Research Council of Norway [Grant 324182 (CA3THY)].

Data availability. The ERA5 datasets are obtained from https://cds.climate.copernicus.eu/datasets. The PDRMIP data can be accessed through the World Data Center for Climate (WDCC) data server at https://doi.org/10.26050/WDCC/PDRMIP_2012-2021. Data of the SyRAP-FORTE2 experiments reported in this paper are available without restriction on reasonable request from Camilla W. Stjern at CICERO Center for International Climate Research.

Author contribution. F. L., M. J., B. H. S. and L. J. W. designed the study. C. W. S., L. J. W., M. J. ran the model simulations. F. L. carried out the analysis and visualized the results. All authors discussed the results and edited the paper.

Competing interests. L. J. W. is a member of the editorial board of *Atmospheric Chemistry and Physics*.

References

Bai, J., Ai, W., Tang, H., and Zhang, Z.: Detectable anthropogenic influence on the changes in structure of precipitation over China using CMIP6 models, Clim. Dyn., 62, 8899-8911, 2024.

Betts, A. K. and Miller, M. J.: The Betts-Miller scheme, in: The Representation of Cumulus Convection in Numerical Models of the Atmosphere, Chapter 9, edited by: Emanuel, K. A. and Raymond, D. J., Amer. Meteor. Soc., Meteor. Mon., 24, 107-121, 1993.

Blaker, A. T., Joshi, M., Sinha, B., Stevens, D. P., Smith, R. S., and Hirschi, J. J. M.:

https://doi.org/10.5194/egusphere-2026-3301
Preprint. Discussion started: 26 June 2026

536 FORTE 2.0: a fast, parallel and flexible coupled climate model, Geosci. Model
537 Dev., 14, 275-293, 2021.
538 Bollasina, M. A., Ming, Y. and Ramaswamy, V.: Anthropogenic aerosols and the
539 weakening of the South Asian summer monsoon, Science, 334, 502-505, 2011.
540 Chavez, S. P. and Barros, A. P.: Aerosol indirect effects on orographic clouds and
541 precipitation, Front. Earth Sci., 11: 1025266.
542 Dong, B., Wilcox, L., Highwood, E., and Sutton, R.: Impacts of recent decadal changes
543 in Asian aerosols on the East Asian summer monsoon: roles of aerosol–radiation
544 and aerosol–cloud interactions, Clim. Dyn., 53, 3235-3256, 2019.
545 Granier, C., Bessagnet, B., Bond, T., D'Angiola, A., Denier van der Gon, H., Frost, G.
546 J., Heil, A., Kaiser, J. W., Kinne, S., Klimont, Z., Kloster, S., Lamargue, J. F.,
547 Liousse, C., Masui, T., Meleux, F., Mieville, A., Ohara, T., Raut, J. C., Riahi, K.,
548 Schultz, M. G., Smith, S. J., Thompson, A., Aardenne, J., van der Werf, G. R., and
549 van Vuuren, D. P.: Evolution of anthropogenic and biomass burning emissions of
550 air pollutants at global and regionalscales during the 1980–2010 period, Climatic
551 Change, 109, 163-190, 2011.
552 Guo, L., Turner, A. G., and Highwood, E. J.: Impacts of 20th century aerosol emissions
553 on the South Asian monsoon in the CMIP5 models, Atmos. Chem. Phys., 15,
554 6367–6378, https://doi.org/10.5194/acp-15-6367-2015, 2015.
555 Guo, Y., Dong, B., and Zhu, J.: Anthropogenic impacts on changes in summer extreme
556 precipitation over China during 1961-2014: Roles of greenhouse gases and
557 anthropogenic aerosols, Clim. Dyn., 60, 2633-2643, 2023.
558 Hersbach, H., Bell, B., Berrisford, P., Biavati, G., Horányi, A., Muñoz Sabater, J.,
559 Nicolas, J., Peubey, C., Radu, R., Rozum, I., Schepers, D., Simmons, A., Soci, C.,
560 Dee, D., Thépaut, J-N.: ERA5 monthly averaged data on pressure levels from 1940
561 to present, Copernicus Climate Change Service (C3S) Climate Data Store (CDS),
562 2023.
563 Hersbach, H., Comyn-Platt, E., Bell, B., Berrisford, P., Biavati, G., Horányi, A., Muñoz
564 Sabater, J., Nicolas, J., Peubey, C., Radu, R., Rozum, I., Schepers, D., Simmons,

https://doi.org/10.5194/egusphere-2026-3301
Preprint. Discussion started: 26 June 2026

A., Soci, C., Dee, D., Thépaut, J-N., Cagnazo, C., Cucchi, M.: ERA5 post-processed daily-statistics on pressure levels from 1940 to present, Copernicus Climate Change Service (C3S) Climate Data Store (CDS), 2023.

Iles, C. E., Samset, B. H., Sandstad, M., Schuhen, N., Wilcox, L., and Lund, M.: Strong regional trends in extreme weather over the next two decades under high- and low-emissions pathways, Nat. Geosci., 17, 845-850, 2024.

Inness, A., Ades, M., Agustí-Panareda, A., Barré, J., Benedictow, A., Blechschmidt, A.-M., Dominguez, J. J., Engelen, R., Eskes, H., Flemming, J., Huijnen, V., Jones, L., Kipling, Z., Massart, S., Parrington, M., Peuch, V.-H., Razinger, M., Remy, S., Schulz, M., and Suttie, M.: The CAMS reanalysis of atmospheric composition, Atmos. Chem. Phys., 19, 3515-3556, 2019.

IPCC: Climate Change 2021: The Physical Science Basis. Contribution of Working Group I to the Sixth Assessment Report of the Intergovernmental Panel on Climate Change [Masson-Delmotte, V., P. Zhai, A. Pirani, S.L. Connors, C. Péan, S. Berger, N. Caud, Y. Chen, L. Goldfarb, M.I. Gomis, M. Huang, K. Leitzell, E. Lonnoy, J.B.R. Matthews, T.K. Maycock, T. Waterfield, O. Yelekçi, R. Yu, and B. Zhou (eds.)], Cambridge University Press, Cambridge, United Kingdom and New York, NY, USA, 2391 pp., 2021.

Lang, Y., Zhang, J., Zhao, J., Gong, Y., Han, T., Deng, X., and Liu, Y.: Mechanisms and quantification: How anthropogenic aerosols weaken the East Asian summer monsoon, npj Clim. Atmos. Sci., 8, 13, 2025.

Li, Z., Lau, W. K., Ramanathan, V., Wu, G., Ding, Y., Manoj, M. G., Liu, J., Qian, Y., Li, J., Zhou, T., Fan, J., Rosenfeld, D., Ming, Y., Wang, Y., Huang, J., Wang, B., Xu, X., Lee, S. S., Cribb, M., Zhang, F., Yang, X., Takemura, T., Wang, K., Xia, X., Yin, Y., Zhang, H., Guo, J., Zhai, P. M., Sugimoto, N., Babu, S. S., and Brasseur, G. P.: Aerosol and Monsoon Climate Interactions over Asia, Rev. Geophys., 54, 866–929, 2016.

Lin, L., Xu, Y., Wang, Z., Diao, C., Dong, W., and Xie, S.: Changes in extreme rainfall over India and China attributed to regional aerosol-cloud interaction during the

https://doi.org/10.5194/egusphere-2026-3301
Preprint. Discussion started: 26 June 2026

late 20th century rapid industrialization, Geophys. Res. Lett., 45, 7857-7865, 2018.

Lin, L., Wang, Z., Xu, Y., and Fu, Q.: Sensitivity of precipitation extremes to radiative forcing of greenhouse gases and aerosols, Geophys. Res. Lett., 43, 9860–9868, 2016.

Liu, L., Shawki, D., Voulgarakis, A., Kasoar, M., Samset, B. H., Myhre, G., Forster, P. M., Hodnebrog, Ø, Sillmann, J., Aalbergsjø, S. G., Boucher, O., Faluvegi, G., Iversen, T., Kirkevåg, A., Lamarque, J., Olivié, D., Richardson, T., Shindell, D. and Takemura, T.: A PDRMIP Multimodel Study on the Impacts of Regional Aerosol Forcings on Global and Regional Precipitation, J. Climate, 31, 4429-4447, 2018.

Luo, F., Samset, B. H., Stjern, C. W., Joshi, M., Wilcox, L. J., Allen, R. J., Hua, W., and Li, S.: Physical processes influencing the Asian climate due to black carbon emission over East Asia and South Asia, Atmos. Chem. Phys., 25, 7647–7667, https://doi.org/10.5194/acp-25-7647-2025, 2025.

Luo, F., Dong, B., Tian, F., and Li, S.: Anthropogenically forced decadal change of South Asian summer monsoon across the mid-1990s, J. Geophys. Res.-Atmos., 124, 806–824, 2019.

Ma, S., Zhou, T., Stone, D., Polson, D., Dai, A., Stott, P., Storch, H., Qian, Y., Burke, C., Wu, P., Zou, L., and Ciavarella, A.: Detectable Anthropogenic Shift toward Heavy Precipitation over Eastern China, J. Climate, 30, 1381-1396, 2017.

Monerie, P. A., Wilcox, L. J., and Turner, A. G.: Effects of anthropogenic aerosol and greenhouse gas emissions on Northern Hemisphere monsoon precipitation: Mechanisms and uncertainty, J. Climate, 35, 2305–2326, 2022.

Muller, C. J. and O'Gorman, P. A.: An energetic perspective on the regional response of precipitation to climate change, Nat. Climate Change, 1, 266-271, 2011.

Myhre, G., Forster, P., Samset, B., Hodnebrog, Ø, Sillmann, J., Aalbergsjø, S. G., Andrews, T., Boucher, O., Faluvegi, G. and Flächner, D.: PDRMIP: A precipitation driver and response model intercomparison project, protocol and preliminary results, B. Am. Meteorol. Soc., 98, 1185-1198, 2017.

https://doi.org/10.5194/egusphere-2026-3301
Preprint. Discussion started: 26 June 2026

623 Riahi, K., Rao, S., Krey, V., Cho, C., Chirkov, V., Fischer, G., Kindermann, G.,
624 Nakicenovic, N., Rafaj, P.: Rcp 8.5—A scenario of comparatively high greenhouse
625 gas emissions, Climatic Change, 109, 33-57, 2011.
626 Richardson, T. B., Forster, P. M., Andrews, T. and Parker, D.: Understanding the rapid
627 precipitation response to CO2 and aerosol forcing on a regional scale, J. Climate,
628 29, 583-594, 2016.
629 Rosenfeld, D., Lohmann, U., Raga, G. B., O'Dowd, C. D., Kulmala, M., Fuzzi, S.,
630 Reissell, A., and Andreae, M. O.: Flood or Drought: How Do Aerosols Affect
631 Precipitation?, Science, 321, 5894, 1309-1313, 2008.
632 Samset, B., Sand, M., Smith, C., Bauer, S., Forster, P., Fuglestvedt, J., Osprey, S., and
633 Schleussner, C.: Climate Impacts from a Removal of Anthropogenic Aerosol
634 Emissions, Geophys. Res. Lett., 45, 1020-1029, 2018.
635 Stjern, C., Joshi, M., Wilcox, L., Gollo, A. and Samset, B.: Systematic Regional Aerosol
636 Perturbations (SyRAP) in Asia using the intermediate-resolution global climate
637 model FORTE2, J. Adv. Mod. Earth System, accepted, 2024.
638 Tian, F., Dong, B., Robson, J. and Sutton, R.: Forced decadal changes in the East Asian
639 summer monsoon: the roles of greenhouse gases and anthropogenic aerosols, Clim.
640 Dynam., https://doi.org/10.1007/s00382-018-4105-7, 2018.
641 Wang, P., Yang, Y., Xue, D., Ren, L., Tang, J., Leung, L., and Liao, H.: Aerosols
642 overtake greenhouse gases causing a warmer climate and more weather extremes
643 toward carbon neutrality, Nat. Commun., 14, 7257, 2023.
644 Webb, D. J.: An ocean model code for array processor computers, Comput. Geosci., 22,
645 569-578, 1996.
646 Wilcox, L. J., Liu, Z., Samset, B. H., Hawkins, E., Lund, M. T., Nordling, K., Undorf,
647 S., Bollasina, M., Ekman, A. M. L., Krishnan, S., Merikanto, J., and Turner, A. G.:
648 Accelerated increases in global and Asian summer monsoon precipitation from
649 future aerosol reductions, Atmos. Chem. Phys., 20, 11955–
650 11977, https://doi.org/10.5194/acp-20-11955-2020, 2020.
651 Wilcox, L. J., Highwood, E. J., Booth, B. B. B., and Carslaw, K. S.: Quantifying sources

https://doi.org/10.5194/egusphere-2026-3301
Preprint. Discussion started: 26 June 2026

of inter-model diversity in the cloud albedo effect, Geophys. Res. Lett., 42, 1568–1575, 2015.

Yang, Y., Li, S. X., and Liao, H.: Impacts of changes in anthropogenic aerosols on precipitation over China during the past four decades, Trans. Atmos. Sci., 49, 147-155, 2026.

Zhao, A. D., Stevenson, D. S. and Bollasina, M. A.: The role of anthropogenic aerosols in future precipitation extremes over the Asian Monsoon Region, Clim. Dyn., 52, 6257–6278, 2019.

Zhao, C., Sun, Y., Yang, J., Li, J., Zhou, Y., Yang, Y., Fan, H., and Zhao, X.: Observational evidence and mechanisms of aerosol effects on precipitation, Sci. Bull., 69, 1569–1580, 2024.

Zhong, W. Y. and Haigh, J. D.: Improved broad-band emissivity parameterization for water vapor cooling calculations, J. Atmos. Sci., 52, 124-148, 1995.

Zou, A., Yang, Y., Wang, H., Wang, P., and Liao, H.: Aerosol decline accelerates the increasing extreme precipitation in China, Geophys. Res. Lett., 52, e2024GL113887, 2025.

https://doi.org/10.5194/egusphere-2026-3301
Preprint. Discussion started: 26 June 2026

669 **Table 1.** Summary of SyRAP-FORTE2 simulations used in the study

Experiment	Name	Aerosol (aerosol effects included)	GHG
Baseline	piC	No aerosol	Pre-industrial climate conditions (280 ppmv, piC)
Perturbation[a]	SO_4_piC	Asian[b] SO_4 AOD (ACI+ARI)[c]	
	ARI_piC	Asian SO_4 AOD (ARI-only)	
	ACI_piC	Asian SO_4 AOD (ACI-only)	
Baseline	p1K	No aerosol	Pre-industrial +1K climate conditions (500 ppmv, p1K)
Perturbation	SO_4_ p1K	Asian SO_4 AOD (ACI+ARI)	
	ARI_ p1K	Asian SO_4 AOD (ARI-only)	
	ACI_ p1K	Asian SO_4 AOD (ACI-only)	

670 a. All of the perturbation simulations are forced by observationally constrained
671 (CAMSRA) repeating monthly sulfate AOD climatologies from 2003-2021
672 b. 60°-140°E, 0°-53°N
673 c. ACI: aerosol-cloud interactions; ARI: aerosol-radiation interactions

https://doi.org/10.5194/egusphere-2026-3301
Preprint. Discussion started: 26 June 2026

674 **Table 2.** Details of the five models in PDRMIP

Model	Resolution (lon × lat)	Level	Aerosol setup
CESM1-CAM5	2.5° × 1.9°	30 levels	CMIP5 Emissions (year 2005)
GISS-E2-R	2.5° × 2°	40 levels	AeroCom Phase II concentrations
HadGEM3	1.875° × 1.25°	85 levels	AeroCom Phase II concentrations
MIROC-SPRINTARS	1.4° × 1.4°	40 levels	HTAP2 emissions (year 2010)
NorESM1	2.5° × 1.9°	26 levels	AeroCom Phase II concentrations

675

676

https://doi.org/10.5194/egusphere-2026-3301
Preprint. Discussion started: 26 June 2026

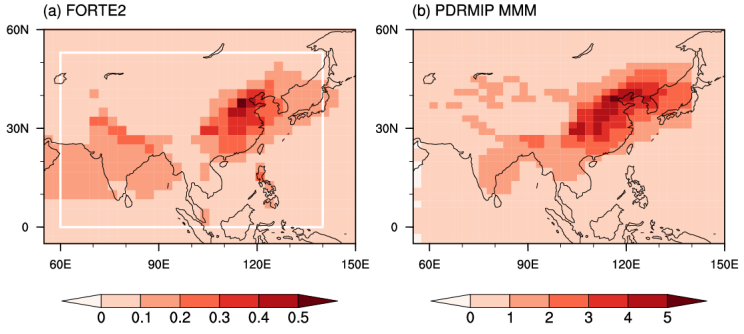

677

678 **Figure 1.** Summer (June-August) sulfate AOD spatial patterns in (a) FORTE2 and (b)
679 PDRMIP MMM. The white box marks the Asian region (60°-140°E, 0°-53°N), over
680 which ACI is parameterized for sulfate perturbations in FORTE2.

681

https://doi.org/10.5194/egusphere-2026-3301
Preprint. Discussion started: 26 June 2026

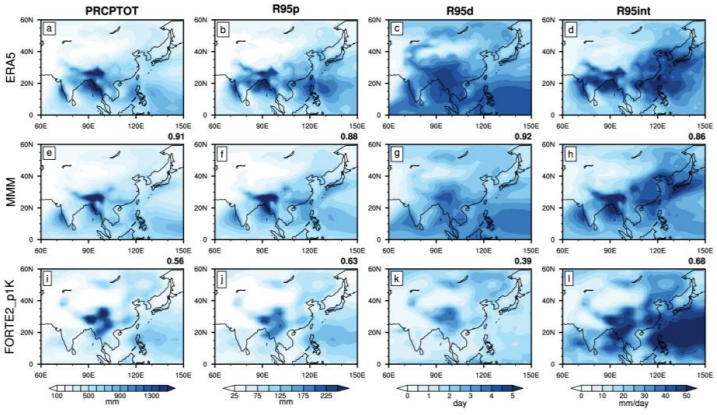

682

683 **Figure 2.** Comparison of climatological summer (June-August) PRCPTOT (mm),
684 R95p (mm), R95d (day) and R95int (mm/day) from (a-d) ERA5 (1981–2010), (e-h) the
685 PDRMIP MMM baseline simulation and (i-l) the FORTE2 p1K baseline simulation.
686 The numbers in the upper right corner represent the spatial correlation coefficients
687 between the models and ERA5.

688

https://doi.org/10.5194/egusphere-2026-3301
Preprint. Discussion started: 26 June 2026

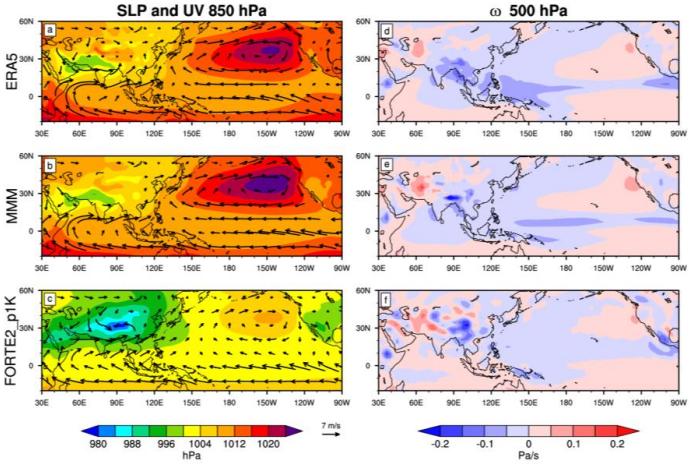

Figure 3. Comparison of climatological summer (a-c) SLP (hPa), 850 hPa horizontal winds (m s^{-1}) and (d-f) 500 hPa vertical winds (ω) (Pa s^{-1}) from ERA5 (1981–2010), the PDRMIP MMM baseline simulation and the FORTE2 p1K baseline simulation.

https://doi.org/10.5194/egusphere-2026-3301
Preprint. Discussion started: 26 June 2026

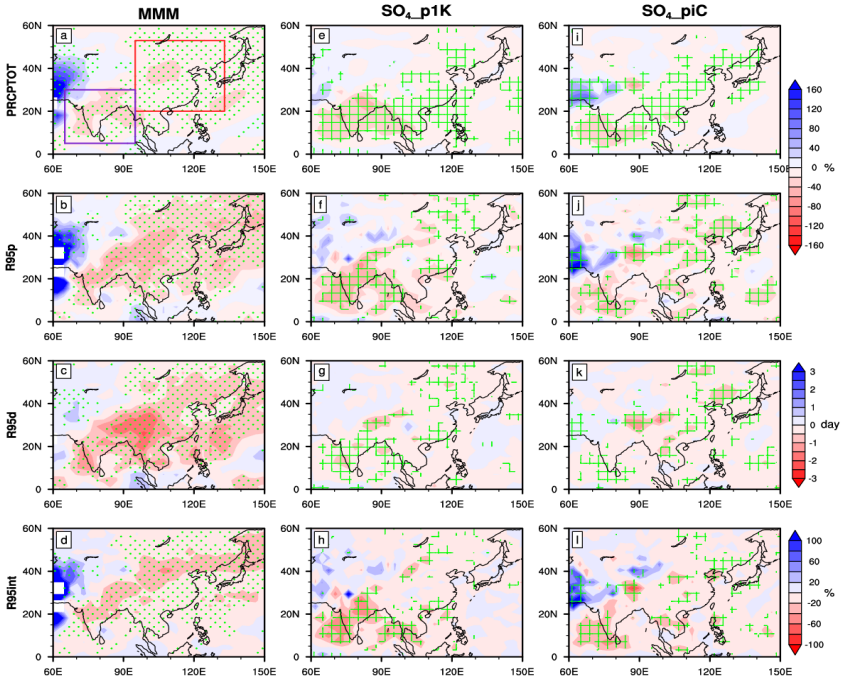

694

695 **Figure 4.** Spatial patterns of summer PRCPTOT (%), R95p (%), R95d (day) and R95int
696 (%) responses to Asian SO_4 aerosol forcing, for (a-d) MMM, (e-h) SO_4_p1K, and (i-l)
697 SO_4_piC. Green dots in MMM denote signals where at least three models agree. Green
698 grid lines in (e-l) indicate regions where responses are statistically significant above the
699 90% level based on a two-tailed Student's t test. The red and purple boxes in (a)
700 delineate East Asia (EAS: 95°E–133°E, 20°N–53°N) and South Asia (SAS: 65°E–95°E,
701 5°N–30°N), respectively.

702

https://doi.org/10.5194/egusphere-2026-3301
Preprint. Discussion started: 26 June 2026

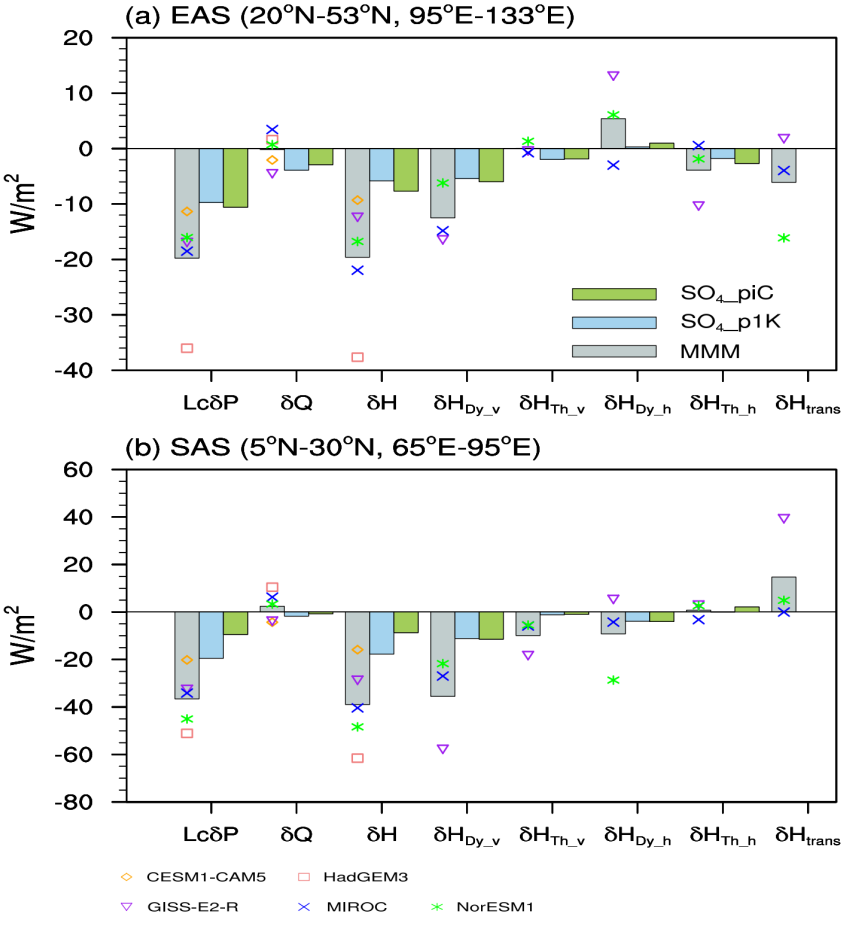

Figure 5. Summer area-averaged responses of the atmospheric energy budget terms over (a) East Asia (EAS) and (b) South Asia (SAS) for the MMM (gray bars), SO_4_p1K (blue bars), and SO_4_piC (green bars). The symbols indicate the individual results from the five PDRMIP models. Note that only three of the five models are used for the decomposition analysis of δH (Eq. 2) due to data availability. Unit: W m^{-2}

https://doi.org/10.5194/egusphere-2026-3301
Preprint. Discussion started: 26 June 2026

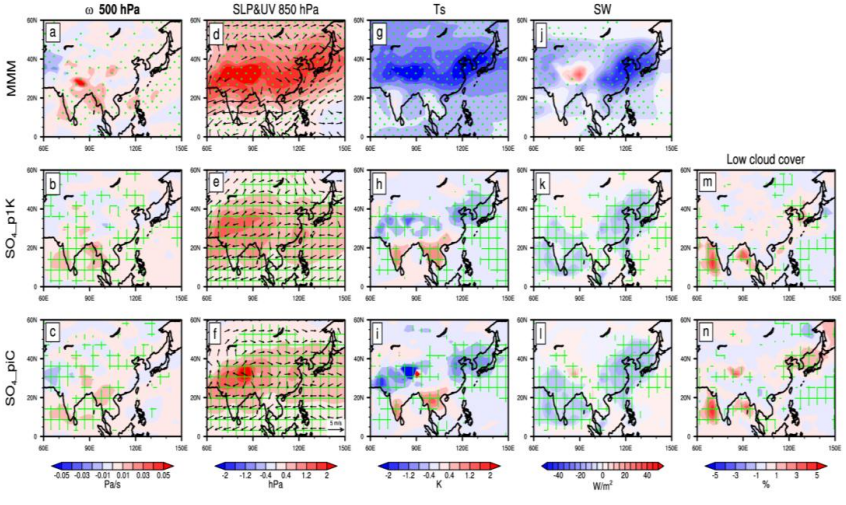

Figure 6. Summer spatial patterns of responses to Asian SO_4 aerosol forcing for the MMM, SO4_p1K, and SO4_piC: (a–c) ω at 500 hPa (Pa s^{-1}), (d–f) sea level pressure (SLP; hPa) and 850-hPa horizontal wind (m s^{-1}), (g–i) surface temperature (T_s; K), (j–l) net surface shortwave radiation (W m^{-2}), and (m–n) low cloud cover (%) for SO4_p1K and SO4_piC only. Green dots in the MMM panels denote signals where at least three models agree. Green grid lines indicate regions where the responses are statistically significant above the 90% confidence level based on a two-tailed Student's t-test.

https://doi.org/10.5194/egusphere-2026-3301
Preprint. Discussion started: 26 June 2026

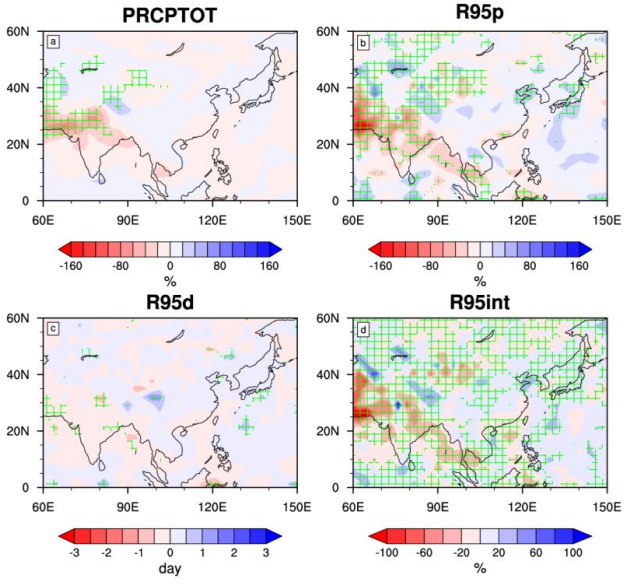

Figure 7. Spatial patterns of summer differences in responses to Asian SO_4 aerosol forcing between the p1K and piC climate states for (a) PRCPTOT (%), (b) R95p (%), (c) R95d (day), and (d) R95int (%). For PRCPTOT, R95p, and R95int, the difference is calculated as the relative response under p1K minus that under piC, i.e., [(SO_4_p1K − p1K)/p1K − (SO_4_piC − piC)/piC]; for R95d, the difference is the absolute response under p1K minus that under piC, i.e., (SO_4_p1K − p1K) − (SO_4_piC − piC). Green grid lines indicate regions where the differences are statistically significant above the 90% confidence level based on a two-tailed Student's t-test.

https://doi.org/10.5194/egusphere-2026-3301
Preprint. Discussion started: 26 June 2026

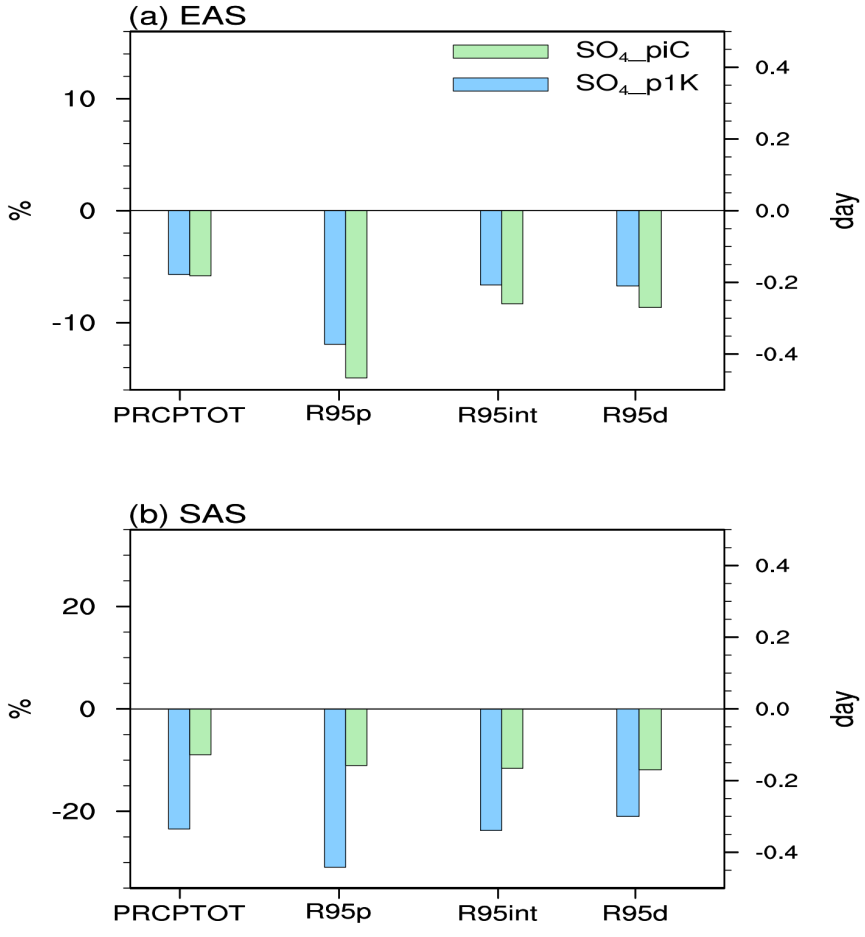

730

731 **Figure 8.** Summer area-averaged responses of PRCPTOT (%), R95p (%), R95d (day),
732 and R95int (%) over (a) East Asia (EAS) and (b) South Asia (SAS) to Asian SO_4 aerosol
733 forcing, shown for SO_4_p1K (blue bars) and SO_4_piC (green bars).

734

https://doi.org/10.5194/egusphere-2026-3301
Preprint. Discussion started: 26 June 2026

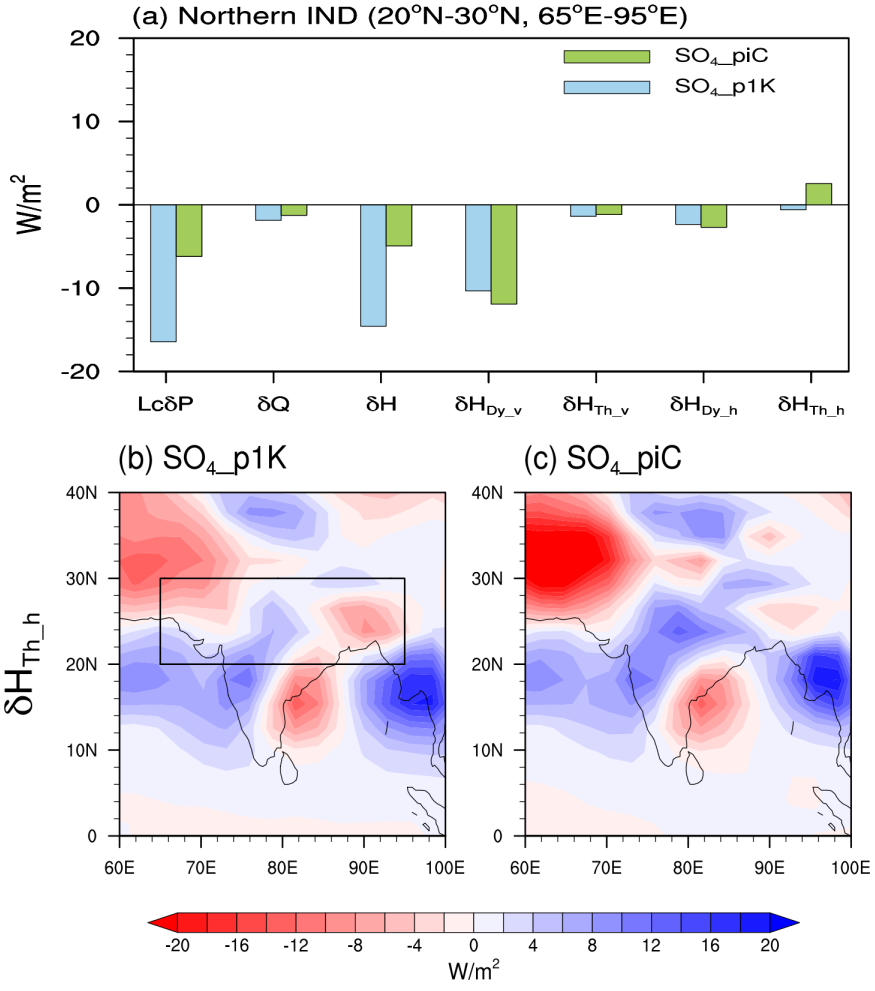

Figure 9. (a) Summer area-averaged responses of the atmospheric energy budget terms over northern India for SO_4_p1K (blue bars) and SO_4_piC (green bars). (b-c) Summer spatial patterns of responses in thermodynamic components with changes in horizontal DSE gradients (δH_{Th_h}) for (b) SO_4_p1K and (c) SO_4_piC. The black box in (b) delineate northern India (65°E–95°E, 20°N–30°N). Units: W m^{-2}

https://doi.org/10.5194/egusphere-2026-3301
Preprint. Discussion started: 26 June 2026

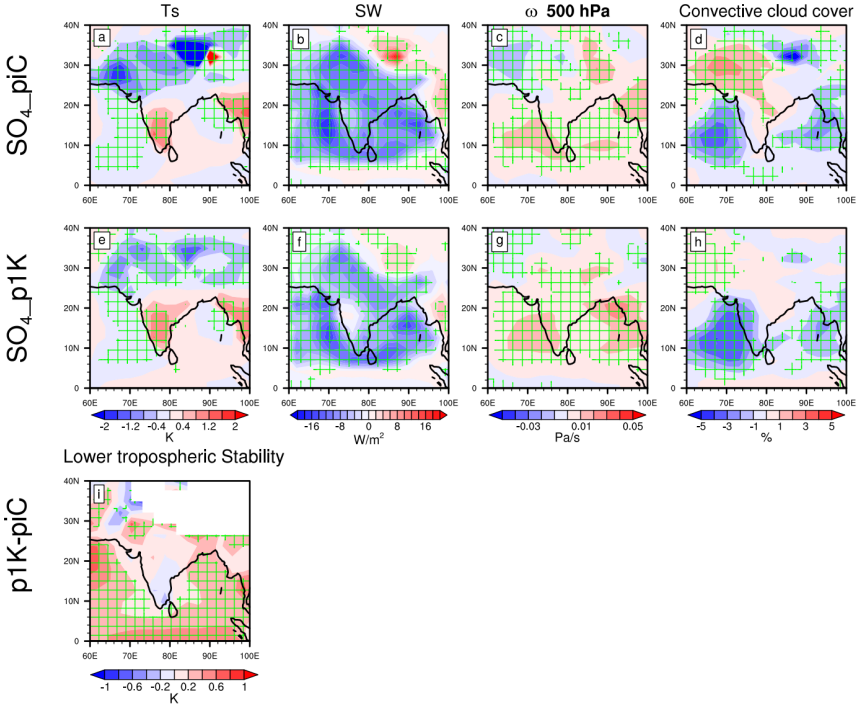

742

743 **Figure 10.** Summer spatial patterns of responses to Asian SO_4 aerosol forcing for
744 SO_4_p1K, and SO_4_piC: (a, e) Ts (K), (b,f) net surface SW (W m^{-2}), (c, g) ω at 500 hPa
745 (Pa s^{-1}), and (d, h) convective cloud cover (%). (i) Differences in lower tropospheric
746 stability (θ_{850}-θ_{sfc}, where θ is potential temperature; K) between p1K and piC (p1K-
747 piC). Green grid lines indicate regions where the responses are statistically significant
748 above the 90% confidence level based on a two-tailed Student's t-test.

749

750

https://doi.org/10.5194/egusphere-2026-3301
Preprint. Discussion started: 26 June 2026

751

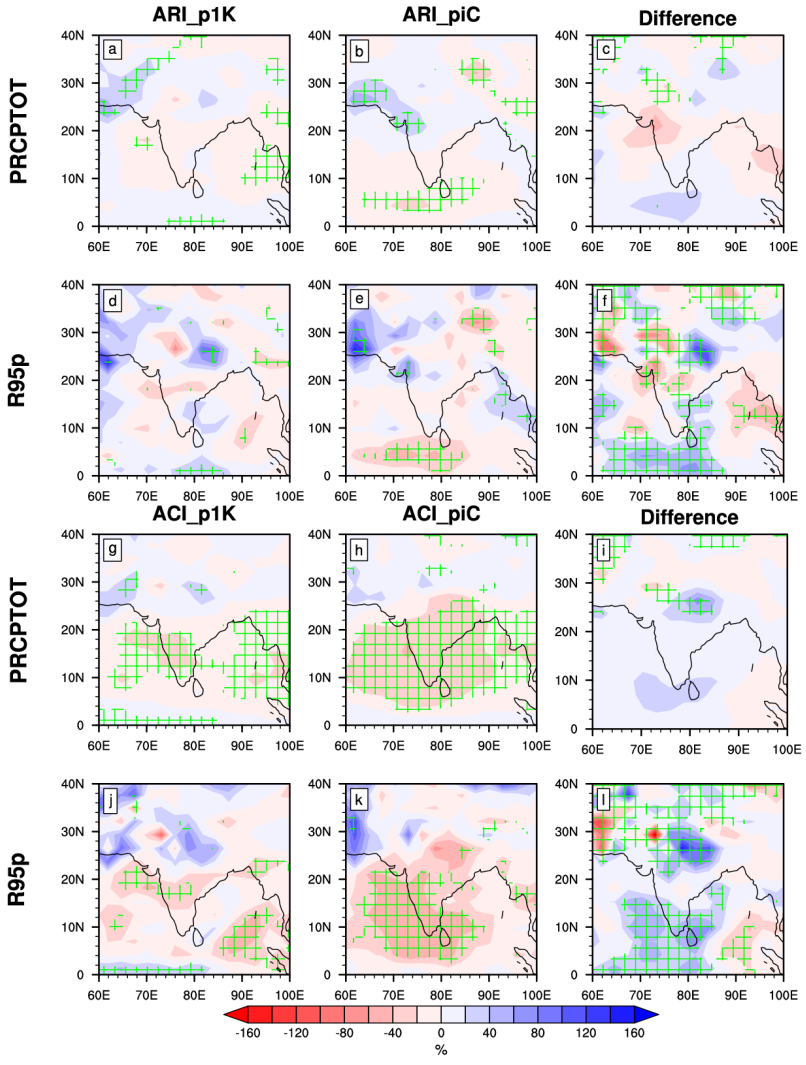

752

753 **Figure 11.** Spatial patterns of summer responses of (a–c) PRCPTOT and (d–f) R95p
754 (%) for ARI_p1K (a, d), ARI_piC (b, e), and the difference in responses between the
755 p1K and piC climate states [(ARI_p1K-p1K)/p1K-(ARI_piC-piC)/piC] (c, f); and for
756 ACI_p1K (g, j), ACI_piC (h, k), and the difference in responses between the present-
757 day and pre-industrial climate [(ARI_p1K-p1K)/p1K-(ARI_piC-piC)/piC] (i, l). Green
758 grid lines indicate regions where responses are statistically significant above the 90%
759 level based on a two-tailed Student's t test.

760

https://doi.org/10.5194/egusphere-2026-3301
Preprint. Discussion started: 26 June 2026

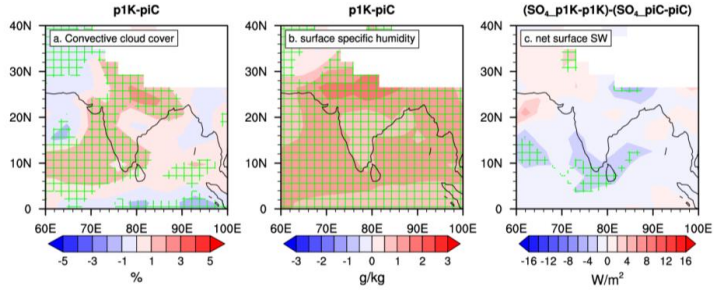

761

762 **Figure 12.** Spatial patterns of summer differences between p1K and piC (p1K- piC) for
763 (a) Convective cloud cover (%) and (b) surface specific humidity (g/kg). (c) Difference
764 in the net surface shortwave radiation (SW) response to Asian SO_4 aerosol forcing
765 between the two climate states (SO_4_p1K − p1K) − (SO_4_piC − piC) (W/m^2). Green
766 grid lines indicate regions where the differences are statistically significant above the
767 90% confidence level based on a two-tailed Student's t-test.

768

https://doi.org/10.5194/egusphere-2026-3301
Preprint. Discussion started: 26 June 2026

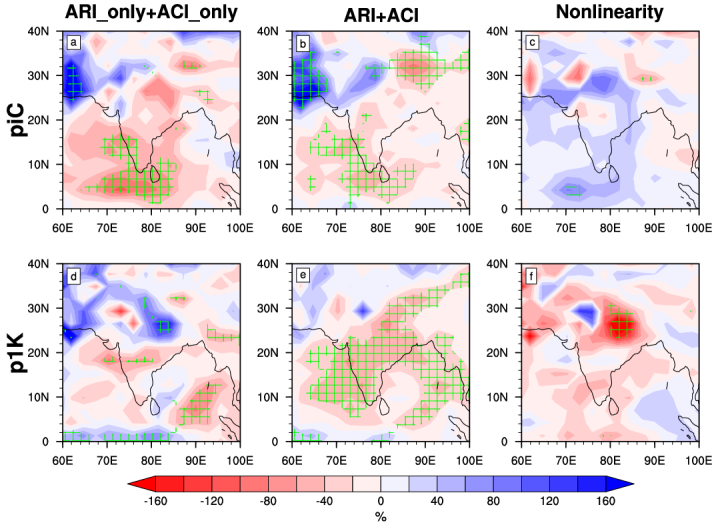

Figure 13. Spatial patterns of summer R95p responses to Asian SO_4 aerosol forcing for the piC (top) and p1K (bottom) climate states: (a, d) sum of the responses from the individual ARI_only and ACI_only simulations, (b, e) response from the combined ARI+ACI simulation, and (c, f) difference between the two [(b, e) minus (a, d)], quantifying the nonlinearity. Green grid lines indicate regions where the differences are statistically significant above the 90% confidence level based on a two-tailed Student's t-test.